

## Optical conductivity, Drude weight and plasmons in twisted graphene bilayers

Tobias Stauber<sup>1</sup>, Pablo San-Jose<sup>2</sup> and Luis Brey<sup>2,3</sup>

<sup>1</sup> Departamento de Física de la Materia Condensada, Instituto Nicolás Cabrera and Condensed Matter Physics Center (IFIMAC), Universidad Autónoma de Madrid, E-28049 Madrid, Spain

<sup>2</sup> Instituto de Ciencia de Materiales de Madrid (ICMM-CSIC), Cantoblanco, E-28049 Madrid, Spain  
E-mail: [brey@icmm.csic.es](mailto:brey@icmm.csic.es)

*New Journal of Physics* **15** (2013) 113050 (20pp)

Received 17 July 2013

Published 26 November 2013

Online at <http://www.njp.org/>

doi:10.1088/1367-2630/15/11/113050

**Abstract.** We numerically calculate the optical conductivity of twisted graphene bilayers within the continuum model. To obtain the imaginary part, we employ the regularized Kramers–Kronig relation, allowing us to discuss arbitrary twist angles, chemical potential and temperature. We find that the Drude weight  $D$  as a function of the chemical potential  $\mu$  closely follows the shell structure of a twisted bilayer displayed by the density of states. For certain angles, this results in a transport gap  $D = 0$  at finite  $\mu$ . We also discuss the loss function which, for low doping, is characterized by acoustic interband ‘plasmons’ and transitions close to the van Hove singularities. For larger doping, the plasmon mode of a decoupled graphene bilayer is recovered that is damped especially for small wave numbers.

<sup>3</sup> Author to whom any correspondence should be addressed.



Content from this work may be used under the terms of the [Creative Commons Attribution 3.0 licence](https://creativecommons.org/licenses/by/3.0/). Any further distribution of this work must maintain attribution to the author(s) and the title of the work, journal citation and DOI.

**Contents**

<b>1. Introduction</b>	<b>2</b>
<b>2. Continuum model of a twisted graphene bilayer</b>	<b>3</b>
<b>3. Linear response theory</b>	<b>6</b>
3.1. Graphene monolayer . . . . .	7
3.2. Twisted bilayer . . . . .	8
<b>4. Optical conductivity</b>	<b>9</b>
<b>5. Drude weight</b>	<b>11</b>
<b>6. Plasmons</b>	<b>14</b>
6.1. Plasmons in twisted bilayer . . . . .	15
6.2. Loss function . . . . .	17
<b>7. Conclusions</b>	<b>18</b>
<b>Acknowledgments</b>	<b>18</b>
<b>References</b>	<b>18</b>

**1. Introduction**

Since the realization that neutral graphene monolayers display a universal optical absorption of  $\pi\alpha \approx 2.3\%$  in the infrared and visible spectrum (with  $\alpha \approx 1/137$  the fine structure constant) [1–4], interest in the interactions between light and graphene has grown rapidly [5–7]. A remarkable aspect of this absorption, other than its suggestive relation to the universal constant  $\alpha$ , is its high value, given the ultimate thinness of a graphene monolayer. In fact, it can be even enhanced up to 10% for photon energies around 4.5 eV due to transitions close to the van Hove singularity [8, 9].

The unique feature of neutral graphene responsible for its strong optical response is the existence of low energy particle–hole interband excitations with zero momentum, by virtue of the gapless Dirac spectrum, that act as an effective sink for photons of arbitrarily low energy. By the same token, all thermally excited plasmons in undoped graphene are damped by this excitation density, but nevertheless remain well-defined [10]. The unique bipolar tunability of graphene further allows one to adjust these optical properties quite simply, by shifting the Fermi energy  $\mu$  away from the Dirac point, be it electrostatically or through chemical doping. This opens a gap of energy  $2\mu$  in the particle–hole excitations, making graphene transparent below this energy, useful, e.g. for broadband optical modulation [11]. It also allows for the emergence of undamped plasmons [12–16].

The spectral features involved in the unusual optical properties outlined above are also present in graphene bilayers [17]. These are often classified according to their stacking, which in the absence of strain have three possible (meta) stable configurations: AB'-type (or BA', also known as Bernal stacking), AA'-type and twisted. The former two are minimal stackings (unit cell with only four carbon atoms) in which half or all sites in opposite layers are vertically aligned, respectively. The twisted bilayer is the most generic type, and is defined by a relative rotation of angle  $\theta$  between the two layers. Each of the three stacking types exhibits a different low energy electronic structure, although all three react strongly to light like the monolayer. The twisted bilayer, however, and in particular the case of low twist angles (around and

below  $1^\circ$ ), has the richest optical response, a consequence of its complex low energy spectral properties. The response, moreover, is highly tuneable through the angle  $\theta$ , an additional control parameter not available in the other graphenes. As a striking example, the strong frequency-dependence of twisted bilayer conductivity and thus reflectivity leads to a visible coloration under white light, that varies with angle  $\theta$ , of flakes on 100 nm thick  $\text{SiO}_2$ , as recently observed experimentally [18].

In this work we study the optical response of twisted graphene bilayers at different twist angles and temperature responsible for this effect. We analyze its optical conductivity at and away from neutrality, the Drude weight and plasmon spectrum. Some of these aspects, specifically the real part of the conductivity, have been studied in recent works for large-angle twisted bilayers [19, 20]. We will make connection with these, and extend them into the low angle regime.

The paper is organized as follows. In section 2, we introduce the continuum model of twisted graphene bilayer and discuss the electronic structure. In section 3, we introduce the Kubo formalism and also comment on the regularization of the Kramers–Kronig relation for the conductivity, necessary in the case of unbounded Dirac fermions. In sections 4 and 5, we present our results for the optical conductivity and the related Drude weight for different angles, chemical potential and temperature. In section 6, we discuss the plasmonic spectrum based on the local conductivity by plotting the energy loss function and close with conclusions.

## 2. Continuum model of a twisted graphene bilayer

Twisted graphene bilayers are a peculiar structure from a crystallographic point of view, since for a generic (non-commensurate) angle the lattice is not exactly periodic, although crystalline order within each layer is extraordinarily robust. This is a consequence of the highly anisotropic binding forces in these systems, also characteristic of graphite. In principle only commensurate twist angles  $\theta = \theta_{mn}$ , where [21]

$$\cos(\theta_{mn}) = \frac{3m^2 + 3mn + n^2/2}{3m^2 + 3mn + n^2} \quad (1)$$

for integer  $m, n$  are amenable to band structure calculations by application of the Bloch theorem.

It turns out, however, that the bandstructure at low energies depends continuously on the value of the angle  $\theta_{n,m}$  itself, not on the specific  $n$  and  $m$  (note that the set of possible commensurate angles  $\theta_{mn}$  is dense). This is a consequence of the fact that the physical interlayer distance  $d > 0.3$  nm is greater than the intralayer carbon–carbon distance  $a_{cc} = 0.14$  nm. In this regime, all properties associated to precise commensurability are efficiently averaged out using microscopic tight-binding models. Consequently, a simple, low energy continuum theory can be formulated that may be applied to an arbitrary twist angle  $\theta$ , and obviates all crystallographic complications to a very good approximation [21, 22].

The first ingredient in the continuum model is the momentum shift between Dirac cones in different layers due to the rotation,  $\Delta K = 2|K|\sin(\theta/2)$ , where  $|K| = 4\pi/3a_0$  and  $a_0 = \sqrt{3}a_{cc}$  is the monolayer Bravais period. The second non-trivial ingredient is the smooth spatial modulation in the interlayer coupling. The twist  $\theta$  produces a triangular Moiré pattern in the local stacking, of period  $L_M = a_0/[2\sin(\theta/2)]$ , see figure 1(a). Hence, the coupling between layers becomes position dependent. The modulation is smooth on the scale  $a_0$ , so the two valleys in each layer remain decoupled in the twisted bilayer. For each valley, the continuum

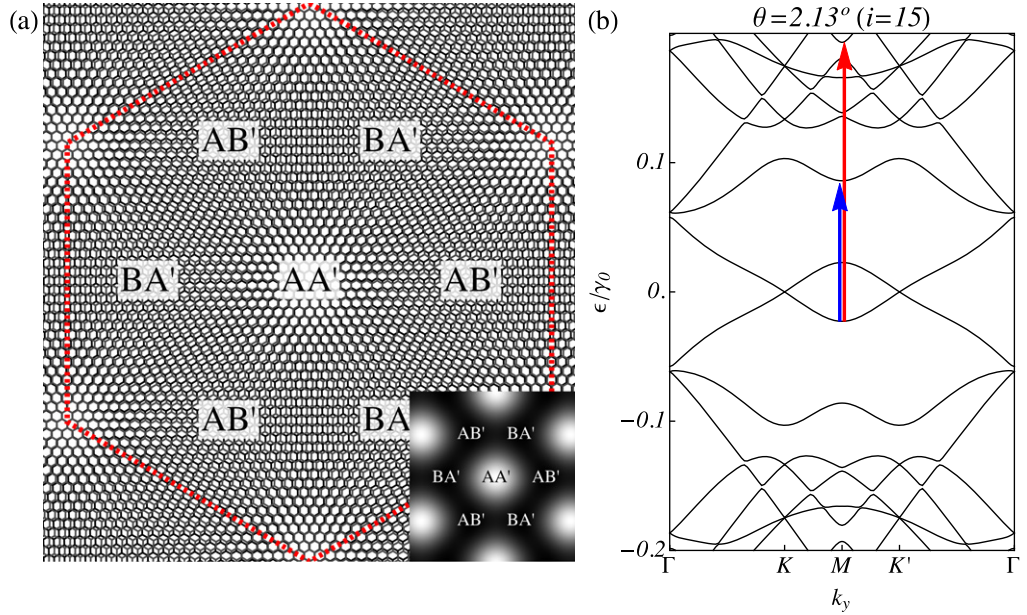


**Figure 1.** (a) Moiré pattern of a bilayer of index  $i = 15$  (conf. equation (4)). Red hexagon denotes the Moiré unit cell. Panel (b) shows the corresponding low energy bandstructure, exhibiting a van Hove singularity at the  $M$  point around  $\epsilon = 0.02\gamma_0$ . The eigenstates at these points are typically localized around the  $AA'$ -stacked regions (inset in (a)). The transitions shown by arrows in (b) correspond to peaks in the optical conductivity marked in figure 3(b).

model Hamiltonian reads [21, 23, 24]

$$H = \begin{pmatrix} 0 & \hbar v_F \Pi_+^\dagger & V^*(\mathbf{r}) & V^*(\mathbf{r} - \delta\mathbf{r}) \\ \hbar v_F \Pi_+ & 0 & V^*(\mathbf{r} + \delta\mathbf{r}) & V^*(\mathbf{r}) \\ V(\mathbf{r}) & V(\mathbf{r} + \delta\mathbf{r}) & 0 & \hbar v_F \Pi_-^\dagger \\ V(\mathbf{r} - \delta\mathbf{r}) & V(\mathbf{r}) & \hbar v_F \Pi_- & 0 \end{pmatrix}. \quad (2)$$

This matrix is written in the local basis  $A, B, A', B'$  comprised of the two sites in the unit cell of each of the two layers. Here, the Fermi velocity is  $v_F = (\sqrt{3}/2)a_0\gamma_0/\hbar \approx 9 \times 10^5 \text{ m s}^{-1}$  and  $\Pi_\pm = [k_x + i(k_y \mp \Delta K/2)]e^{i\pm\theta/2}$ . The function  $V(\mathbf{r}) = \frac{1}{3}\gamma_\perp \sum_{i=1}^3 e^{i\mathbf{g}_i \cdot \mathbf{r}}$  describes the periodic spatial variation of the interlayer coupling, with  $\gamma_\perp \approx 0.33 \text{ eV}$ . The Moiré lattice vectors are denoted by  $\mathbf{a}_{1,2}$  (so  $L_M = |\mathbf{a}_{1,2}|$ ) and conjugate momenta are  $\mathbf{g}_{1,2}$ , such that  $\mathbf{g}_i \cdot \mathbf{a}_j = 2\pi\delta_{ij}$  (we also define  $\mathbf{g}_3 = 0$ ). The  $AA'$  sublattice is centered at the origin, with the  $AB'/BA'$  sublattices offset given by  $\pm\delta\mathbf{r} = (\mathbf{a}_1 - \mathbf{a}_2)/3$ . These offsets are used in equation (2) to write the sublattice-resolved interlayer coupling so that it alternates in space between  $AB'$ ,  $BA'$  and  $AA'$  types, following the Moiré pattern.

We first review the bandstructure phenomenology of the twisted bilayer. The continuum model has two distinct regimes, denoted as large and small angles, each with very different features. The large angle regime, relevant for  $\theta$  greater than a few degrees, is characterized by two low energy Dirac cones per valley at the superstructure  $K$  and  $K'$ , with a reduced Fermi

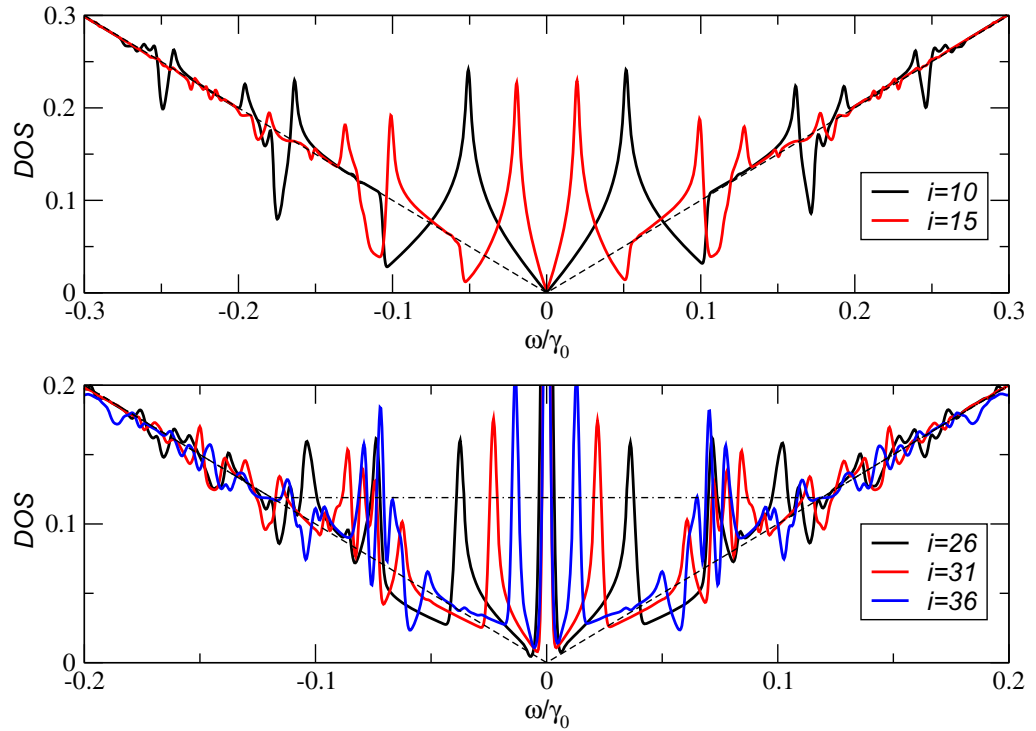


**Figure 2.** DOS for different angles  $\theta_i$  in units of  $\rho_0 = \frac{4\gamma_0}{\pi(\hbar v_F)^2}$ . Upper panel:  $\theta = 3.15^\circ$  (black) and  $\theta = 2.13^\circ$  (red). Lower panel:  $\theta = 1.25^\circ$  (black),  $\theta = 1.05^\circ$  (red) and  $\theta = 0.91^\circ$  (blue). The dashed and dotted-dashed lines resemble the DOS of decoupled bilayer and AA-stacked bilayer, respectively. The index  $i$  is related to the angle by equation (4).

velocity [25–27]

$$v_F^* \approx v_F[1 - 9\alpha^2 + \mathcal{O}(\alpha^4)], \quad (3)$$

where  $\alpha = \gamma_\perp/6\epsilon_M$  is an expansion parameter that represents the dimensionless interlayer coupling and  $\epsilon_M(\theta) = \hbar v_F \Delta K/2 = (2\pi/3)\hbar v_F/L_M$  is the energy scale associated to the Moiré period  $L_M$ . Also, a low-energy van Hove singularity at energy  $\epsilon_{vH} \approx \epsilon_M - \gamma_\perp/3$ , see figure 1(b), is created [23, 28–31].

At an angle  $\theta_1^m \approx 1.05^\circ$ , known as the ‘first magic angle’,  $v_F^*$  becomes zero, the van Hove singularity degenerates into a narrow miniband around zero energy. This is the onset of the small angle regime. From this point on, the electronic structure becomes considerably complex. The Fermi velocity becomes finite again, as the miniband moves away from zero energy. Higher energy van Hove singularities appear and approach zero at subsequent magic angles  $\theta_{2,3,4,\dots}^m$ , where the Fermi energy vanishes once more.

In figure 2, the density of states (DOS) is shown for various angles labeled by the index  $i$

$$\cos(\theta_i) = 1 - \frac{1}{2(3i^2 + 3i + 1)}, \quad (4)$$

obtained from equation (1) with  $m = n + 1 = i$ . The curves are normalized by  $\rho_0 = \frac{4\gamma_0}{\pi(\hbar v_F)^2}$  such that the DOS of two uncoupled graphene layers is just a straight line with slope 1 (dashed line).

Note that the DOS is almost but not exactly symmetric for positive and negative energies as a consequence of the underlying (not electron–hole symmetric) Hamiltonian.

In the upper panel, we show the DOS for ‘large’ angles  $\theta$  with  $i = 10$  (blue) and  $i = 15$  (red). Around the neutrality point, the spectrum is characterized by a van Hove singularity followed by a step singularity, forming a closed shell. For small energies the system is thus approximately described by a hexagonal tight-binding model with renormalized band-width. This shell structure is somehow repeated for larger energies until it fades away and the DOS for decoupled bilayer graphene is recovered. Note that the weight of the van Hove singularity is slightly decreasing with increasing (intermediate)  $i$ .

For small angles around the first magic angle  $\theta_1^m = 1.05^\circ$  ( $i = 31$ , lower panel in figure 2), more distinct van Hove singularities appear and the height of the first van Hove singularity is strongly enhanced with increasing  $i$ . A close-up of this energy regime is shown on the left hand side of figure 8.

### 3. Linear response theory

The above phenomenology in the electronic bandstructure has an associated signature in the optical response of the system as the angle decreases. The basic quantity governing the linear optical response of any electronic system is the optical conductivity  $\sigma_{\alpha\beta}(\omega)$  (where  $\alpha, \beta = x, y$ ), which gives the electric current arising in response to a weak and uniform, time-dependent electric field of frequency  $\omega$ ,  $\mathbf{E}(t) = \mathbf{E}(\omega) e^{i\omega t}$ ,

$$\mathbf{j}_\alpha(\omega) = \sum_\beta \sigma_{\alpha\beta}(\omega) \mathbf{E}_\beta(\omega). \quad (5)$$

The optical conductivity may be written, using linear response theory, in terms of the current response  $\chi_{j_\alpha j_\beta}(\mathbf{q}, \omega)$  at zero-momentum,

$$\sigma_{\alpha\beta}(\omega) = i \frac{e^2}{\omega + i\delta} \chi_{j_\alpha j_\beta}(\mathbf{q} = 0, \omega), \quad (6)$$

where, as is conventional,  $\delta$  denotes a positive infinitesimal. The current response function  $\chi_{j_\alpha j_\beta}$  consists, in general, of two terms: the diamagnetic and the paramagnetic contribution [32]. The general formalism for obtaining the diamagnetic contribution in a tight-binding model is outlined in [33], however, in the continuum model for the twisted bilayer, as in the monolayer, the diamagnetic contribution vanishes due to the fact that  $\partial^2 H / \partial k_\alpha^2 = 0$ . Hence, we have simply the paramagnetic contribution, given by the Kubo formula

$$\chi_{j_\alpha j_\beta}(\mathbf{q}, \omega) = g_s g_v \int \frac{d^2 \mathbf{k}}{(2\pi)^2} \sum_{mn} \frac{n_F(\epsilon_{m,\mathbf{k}}) - n_F(\epsilon_{n,\mathbf{k}+\mathbf{q}})}{\hbar\omega - \epsilon_{n,\mathbf{k}+\mathbf{q}} + \epsilon_{m,\mathbf{k}} + i\delta} \langle m, \mathbf{k} | j_\alpha | n, \mathbf{k} + \mathbf{q} \rangle \langle n, \mathbf{k} + \mathbf{q} | j_\beta | m, \mathbf{k} \rangle. \quad (7)$$

Here,  $g_s = g_v = 2$  are the spin and valley degeneracies. States  $|m, \mathbf{k}\rangle$  are eigenstates of  $H$  in subband  $m$  and of momentum  $\mathbf{k}$  in the first Brillouin zone of the superstructure. Their eigenenergies are  $\epsilon_{m\mathbf{k}}$  and  $n_F$  is the Fermi function. The paramagnetic current operator is  $j_\alpha = -\partial H / \partial k_\alpha$ . In the continuum model with local interlayer coupling, this current does not mix layers and is thus independent of the coupling  $\gamma_\perp$ . For a system with time-reversal symmetry, the conductivity tensor is diagonal and due to the threefold rotational symmetry of



(twisted) bilayer graphene proportional to the unity tensor. We will, therefore, drop the tensor indices in what follows.

The real part of the conductivity  $\sigma(\omega)$  represents the power dissipation of the system upon incidence of light at frequency  $\omega$ , while its imaginary part represents inductive retardation of the current with respect to the driving field. From equation (6), it is obvious that the conductivity is ill-defined at  $\omega = 0$  and  $\delta \rightarrow 0$  if  $\chi_{jj}(\mathbf{q} = 0, \omega = 0) \neq 0$ . It is thus customary to split up the conductivity into a regular part and a term containing the delta-singularity

$$\sigma(\omega) = \pi D \delta(\omega) + \sigma_{\text{reg}}(\omega), \quad (8)$$

$$\sigma_{\text{reg}}(\omega) = \frac{ie^2}{\omega} \chi_{jj}(\mathbf{q} = 0, \omega) \quad (9)$$

with the Drude weight (or charge stiffness)  $D$  defined as

$$D = e^2 \lim_{\omega \rightarrow 0} \text{Re } \chi_{jj}(\mathbf{q} = 0, \omega) = \lim_{\omega \rightarrow 0} \omega \text{Im } \sigma(\omega). \quad (10)$$

Above we used the fact that the imaginary part of the current response is an odd function. We thus have  $\text{Im } \sigma = \text{Im } \sigma_{\text{reg}}$  and will drop the subindex when confusion is unlikely.

### 3.1. Graphene monolayer

In the case of a graphene monolayer [34, 35], described within a continuum Dirac model, we have the famous zero temperature result ( $\mu$  is the chemical potential with respect to the neutrality point)

$$\begin{aligned} \text{Re } \sigma_{\text{reg}}(\gamma_0 \gg \omega > 2\mu) &= \sigma_0 = \frac{\pi e^2}{2h}, \\ \text{Re } \sigma_{\text{reg}}(\omega < 2\mu) &= 0. \end{aligned} \quad (11)$$

This universal value  $\sigma_0$  for the Dirac gas includes valley and spin degeneracy factors, and is valid for energies  $\hbar\omega \sim 1$  eV well below the  $\gamma_0 \sim 3$  eV van Hove singularity of the monolayer. As  $\omega$  approaches this scale, a discrete model must be employed to compute the monolayer  $\sigma_0$  (see [4] for general results).

The imaginary part of the conductivity, in the same limit of low frequencies, reduces to [3, 4]

$$\text{Im } \sigma(\omega \ll \gamma_0) = \frac{4}{\pi} \frac{\mu}{\hbar\omega} \sigma_0 + \frac{1}{\pi} \log \left| \frac{\hbar\omega - 2\mu}{\hbar\omega + 2\mu} \right| \sigma_0, \quad (12)$$

where  $\mu$  is the Fermi energy, measured from the Dirac point (charge neutrality). Using equation (10), we have a Drude weight

$$D_0 = \frac{4\mu}{\pi\hbar} \sigma_0, \quad (13)$$

which vanishes at neutrality. Note that the above expression only scales with the chemical potential and no other material constant (Fermi velocity) is involved. The Drude weight for twisted bilayer as function of  $\mu$  will thus be independent of the twist angle in the regime where the electronic spectrum can be described by a (renormalized) Dirac model. This breaks down close to the first magic twist angle with the emergence of a flat band.

### 3.2. Twisted bilayer

In the more general case of a twisted bilayer, the computation of  $\sigma(\omega)$  becomes a numerical task and it is usually simpler to compute  $\text{Re } \sigma_{\text{reg}}$  than  $\text{Im } \sigma$ , since, by virtue of equation (7), the former reduces to an integral constrained to eigenstates within  $\hbar\omega$  of the Fermi energy

$$\text{Re } \sigma_{\text{reg}}(\omega) = \frac{16\pi\sigma_0}{\omega} \int \frac{d^2\mathbf{k}}{(2\pi)^2} \sum_{mn} [n_F(\epsilon_{n,\mathbf{k}}) - n_F(\epsilon_{m,\mathbf{k}})] |\langle m, \mathbf{k} | j_x | n, \mathbf{k} \rangle|^2 \delta[\omega - (\epsilon_{m,\mathbf{k}} - \epsilon_{n,\mathbf{k}})/\hbar]. \quad (14)$$

The real part of the conductivity differs from that of two decoupled monolayers only at frequencies smaller than or comparable to the interlayer coupling  $\omega < \gamma_\perp$ . Hence we have  $\text{Re } \sigma_{\text{reg}}(\omega \gg \gamma_\perp) \approx 2\sigma_0$ . This result will be useful in the following discussion to obtain a regularized expression for the imaginary part of the conductivity.

To compute the imaginary part, and from that, the Drude weight  $D$  through equation (10), one could in principle employ equation (7). This is problematic, since it involves a summation, even for small  $\omega$ , over the whole band, which in the continuum model extends to infinity. We will, therefore, make use of the Kramers–Kronig (KK) relation, applicable to any response function. In terms of the conductivity, this yields

$$\text{Im } \sigma(\omega) = \frac{2}{\pi\omega} \mathcal{P} \int_0^\infty dv \frac{v^2 \text{Re } \sigma_{\text{reg}}(v)}{\omega^2 - v^2}, \quad (15)$$

where  $\mathcal{P}$  denotes the Cauchy principal value. There is apparently no advantage to using equation (15) as compared to equation (7), since the integral above extends to infinity, too. Moreover, the integral is ill defined, since at high frequencies the continuum model yields a constant  $\text{Re } \sigma_{\text{reg}}(\omega \gg \gamma_\perp) \approx 2\sigma_0$ .

We will thus define the imaginary part relative to this divergent background following the usual procedure of ultraviolet field theories. In fact, this is one way of obtaining equation (17) and was discussed more generally in the context of the  $f$ -sum rule in [36]. The low energy properties are not modified by this regularization and we can simply subtract the ground-state expectation value of the two independent graphene layers at zero doping. Since the imaginary part for the neutral system is zero for the continuum model, the final regularized definition of  $\text{Im } \sigma$  simply reads

$$\text{Im } \sigma(\omega) = \frac{2}{\pi\omega} \int_0^\infty dv \frac{v^2 (\text{Re } \sigma_{\text{reg}}(v) - 2\sigma_0)}{\omega^2 - v^2}. \quad (16)$$

Numerically, equation (16) can be evaluated by introducing a finite cutoff  $\Lambda$  for which  $\text{Re } \sigma_{\text{reg}}(\Lambda) \approx 2\sigma_0$ . Integrating the second term involving the ‘ground-state value’  $2\sigma_0$  then yields the final formula

$$\text{Im } \sigma(\omega) = \frac{2}{\pi\omega} \left( \mathcal{P} \int_0^\Lambda dv \frac{v^2 \text{Re } \sigma_{\text{reg}}(v)}{\omega^2 - v^2} + 2\sigma_0 \Lambda \right) + \frac{2\sigma_0}{\pi} \log \left( \frac{\Lambda - \omega}{\Lambda + \omega} \right). \quad (17)$$

Note that this expression should be independent of  $\Lambda$  as it was obtained from equation (16). The extra terms compared to the original KK-relation (15) can be interpreted as the diamagnetic contribution that naturally arises in the Dirac model with finite band cutoff.

Using this expression, the Drude weight  $D$  in equation (10) may be written as

$$D = \frac{2}{\pi} \left( 2\sigma_0 \Lambda - \int_0^\Lambda dv \text{Re } \sigma_{\text{reg}}(v) \right). \quad (18)$$



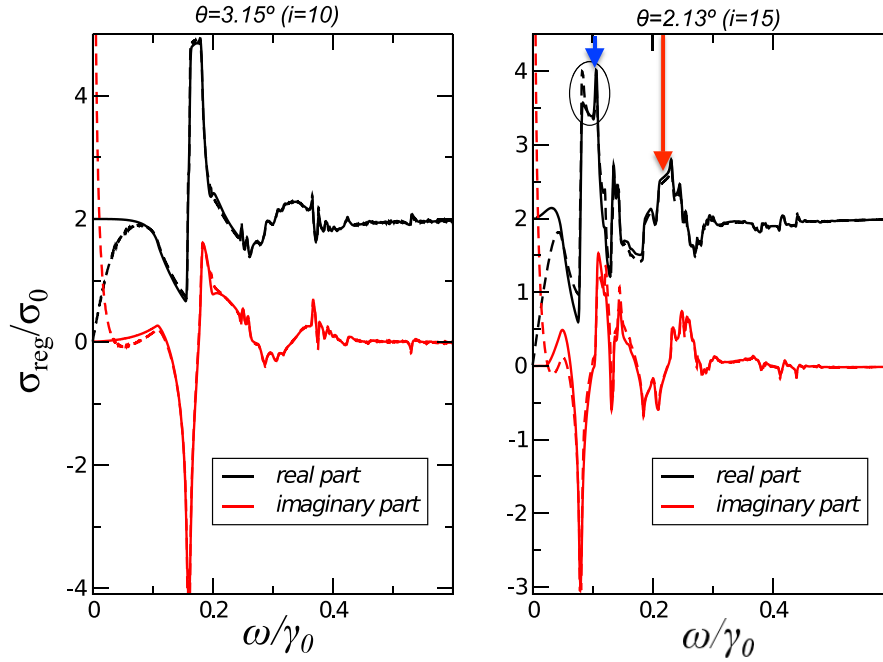


**Figure 3.** Real (black) and imaginary (red) part of the optical conductivity of twisted bilayer graphene at neutrality  $\mu = 0$  for two different angles at  $T = 0$  ( $i = 10$ , left and  $i = 15$ , right). Normalization constants are the universal monolayer conductivity  $\sigma_0 = (\pi/2)e^2/h$ , and  $\gamma_0 = 2.78$  eV. Index  $i$  is related to the angle by equation (4). The dashed lines refer to finite temperature with  $T = 300$  K. Arrows on the right panel correspond to optical transitions in figure 1(b).

This expression, like equation (17), becomes  $\Lambda$ -independent for large cutoffs. In terms of  $D$ , equation (17) is then finally rewritten as

$$\text{Im } \sigma(\omega) = \frac{D}{\omega} + \frac{2\omega}{\pi} \mathcal{P} \int_0^\infty dv \frac{\text{Re } \sigma_{\text{reg}}(v) - 2\sigma_0}{\omega^2 - v^2}. \quad (19)$$

From equation (18), we can also deduce the  $f$ -sum rule

$$\int_0^\Lambda d\omega \text{Re } \sigma(\omega) = 2\sigma_0 \Lambda, \quad (20)$$

which is independent of the angle  $\theta$ , chemical potential  $\mu$  or temperature  $T$ .

#### 4. Optical conductivity

The conductivity at neutrality  $\mu = 0$  is shown in figure 3 for two ‘large’ twist angles. Much like the monolayer, the real part (black) exhibits a universal asymptotic value  $\text{Re } \sigma(\omega \rightarrow 0) = 2\sigma_0$ . It also exhibits signatures of the van Hove singularities, in form of a dip-peak structure as discussed in detail in [19]. The imaginary part (red) exhibits similar features, but vanishes at  $\omega \rightarrow 0$ , i.e. there is no Drude weight at  $\mu = 0$ . This changes for finite temperature where the real part of  $\sigma$  is suppressed for  $\hbar\omega \lesssim k_B T$  [37], as a consequence of the cancelation of the  $n_F$  difference in equation (14). This results in a finite Drude weight, necessary to fulfill the  $f$ -sum

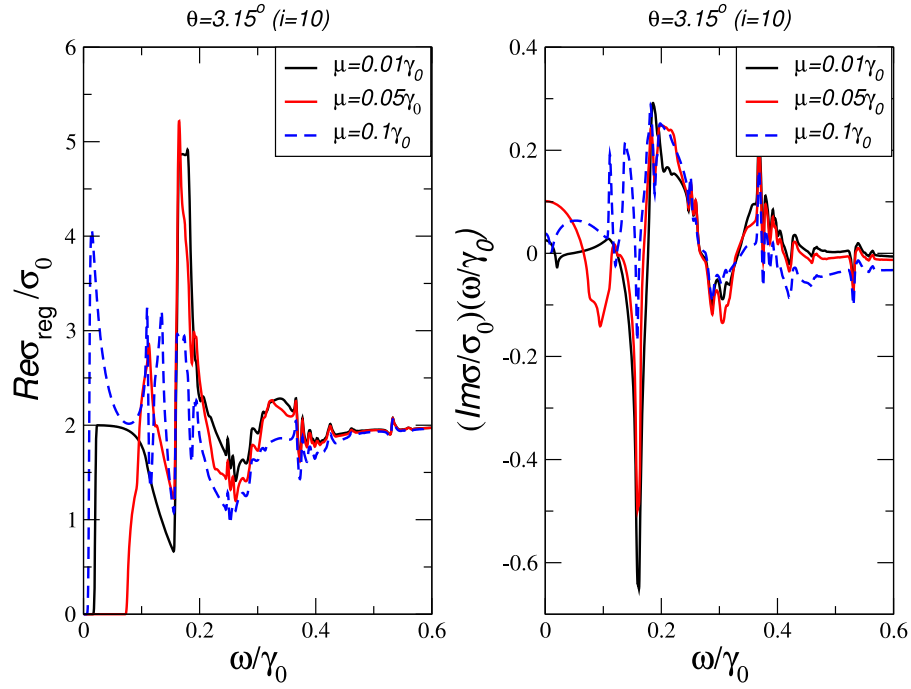


**Figure 4.** Real (left) and imaginary (right) part of the optical conductivity at increasing value of the Fermi energy  $\mu$ , as measured from neutrality for  $\theta = 3.15^\circ$  ( $i = 10$ ). Rest of parameters like on the left hand side of figure 3. Note that  $\text{Im}\sigma(\omega)$  has been multiplied by  $\omega$  to reveal its  $\omega \rightarrow 0$  asymptotics.

rule equation (20). The Drude weight for finite temperature can be deduced from equation (13) with the substitution  $\mu \rightarrow 2 \ln 2k_B T$  [38]. Note that increasing temperature merely changes the Drude weight (figure 7), not the width of the Drude peak, i.e.  $\text{Re}\sigma_{\text{reg}}(\omega \rightarrow 0) = 0$  at finite  $T$ . Temperature can further cause a shift of spectral weight close to the transitions associated to the van Hove singularity (see the circled region), creating new peaks that are absent at zero temperature.

In the case of finite doping  $\mu \neq 0$ , see figure 4, the imaginary part of the conductivity develops a  $\sim D(\mu)/\omega$  low frequency divergence, while the real part becomes suppressed below a threshold frequency  $2\mu$  for small enough  $\mu$  (see black and red curves). Unlike for the monolayer, however, this is only true for  $\mu$  below the van Hove singularity, since it relies on the linearity of the bandstructure (and DOS) around  $\mu = 0$ . For chemical potentials close to the van Hove singularity, i.e.  $\mu \approx \epsilon_M$ , the optical gap is again filled by spectral weight and the Drude weight reduces consistent with the  $f$ -sum rule (blue dashed curves). At finite temperature, the optical gap may persist for small twist angle and the Drude weight can thus even increase, see figure 7.

For large chemical potentials  $\mu \gg \epsilon_M$ , the electronic spectrum (DOS) of the continuum model is just that of two uncoupled graphene layers and one could thus expect to recover the conventional graphene conductivity. But the Moiré coupling between layers induces additional damping, since it opens up the possibility of more interband dissipation channels, i.e. any particle-hole excitation with momentum equal to a multiple of the momenta of the Moiré lattice. In order to understand the basic features of the conductivity on the basis of the uncoupled system, we can thus attribute a finite in-plane wavenumber  $q \sim n\Delta K$  to the incoming photon

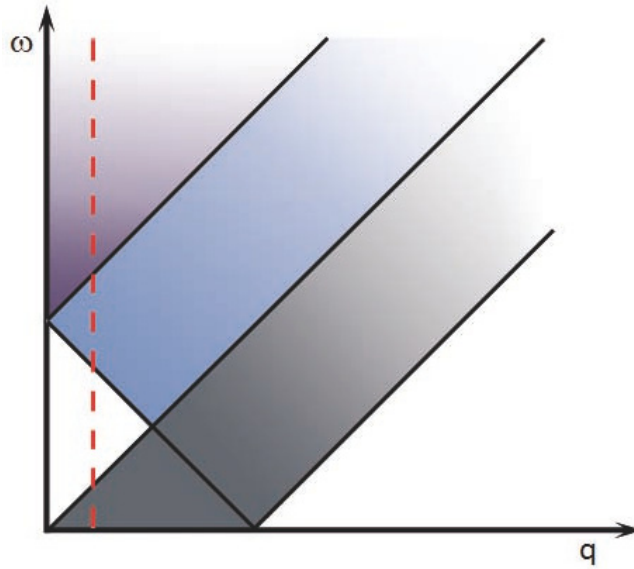


**Figure 5.** Two particle spectrum of pristine graphene. Black shaded regions correspond to intraband transitions, whereas blue and violet shaded regions indicate interband transitions. The red vertical line denotes processes with finite momentum  $q$ .

( $n > 0$ ), see figure 5. The two-particle spectrum of interband and intraband excitations then predicts dissipation at low energies (black) and a broadened transition (blue) from the optical gap to the universal value  $2\sigma_0$  of the conductivity.

In figure 6, the optical conductivity at the first magic angle  $i = 31$  is shown for various chemical potentials (solid lines) and compared to  $\text{Re } \sigma_{\text{reg}}$  for  $i = 10$  (dashed blue line). For low chemical potential, the optical response differs considerably for small and large angles, but for increasing  $\mu$  the dependence on the twist angle becomes less and  $\text{Re } \sigma$  is characterized by a large Moiré-broadening of the optical gap around  $\hbar\omega = 2\mu$ . Still, there is the pronounced spectral weight at  $\hbar\omega = \epsilon_{\text{vH}}$  almost independent of  $\mu$ , which is especially striking for larger angles. This feature cannot be explained from figure 5 and is twist angle dependent.

## 5. Drude weight

Considering only intraband transitions of one unbounded conduction band, the Drude weight or charge stiffness is proportional to the chemical potential, independent of its dispersion relation. For parabolic band electrons,  $D$  is thus simply related to the charge density,  $D = e^2 n/m$ , whereas for Dirac Fermions one gets  $D \sim \sqrt{n}$ , see equation (13). In systems with a finite band-width, we expect a non-monotonous behavior expressing the fact that the Fermi energy is first related to electrons and later to holes when sweeping the chemical potential through the band. For the one-dimensional tight-binding model, one finds, e.g.  $D \sim \sqrt{1 - (\mu/2\gamma_0)^2}$  with  $2\gamma_0$  the band width. For the two-dimensional (2D) hexagonal tight-binding model, the system is characterized by a van Hove singularity at  $\mu = \gamma_0$  around which the Drude weight shows a maximum [37].

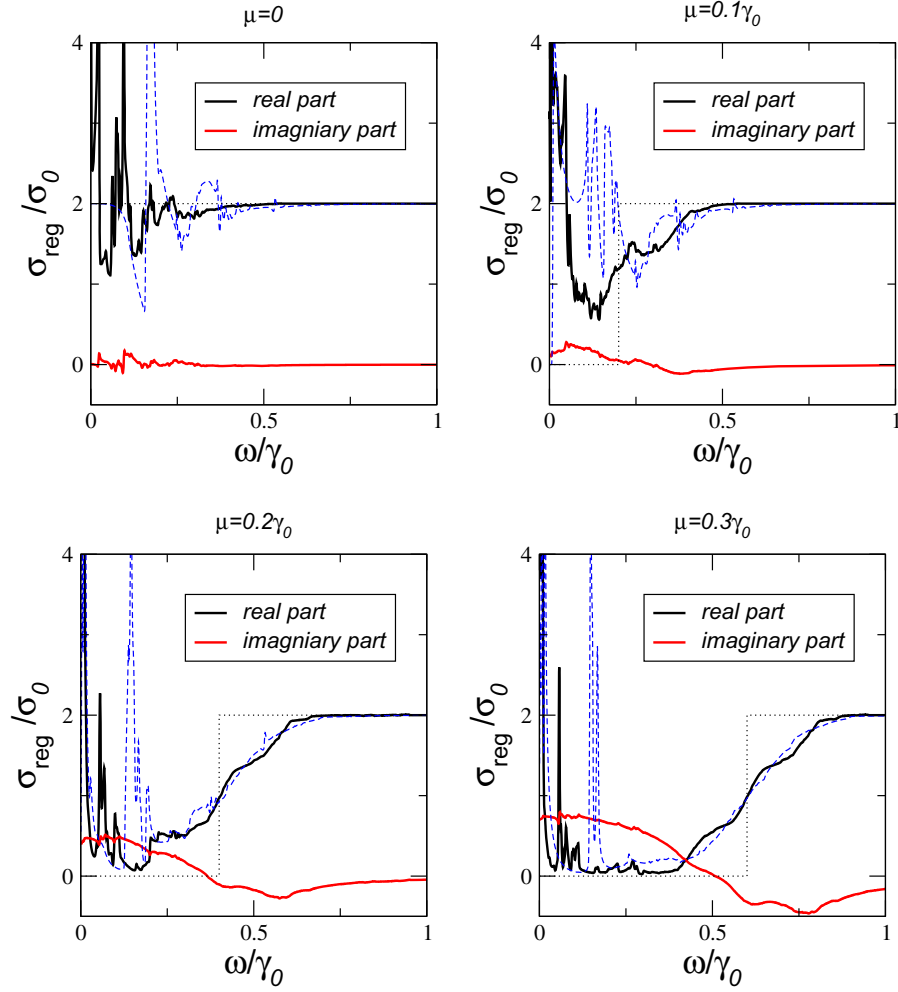


**Figure 6.** Real (black) and imaginary (red) part of the optical conductivity for different chemical potential  $\mu$  at the first magic angle  $\theta_1^m = 1.05^\circ$  ( $i = 31$ ). Rest of parameters like in figure 3. For comparison, also  $\text{Re } \sigma$  for ( $i = 10$ ) is shown (dashed blue line). Dotted lines resemble the limit for uncoupled layers. Note that  $\text{Im } \sigma(\omega)$  has been multiplied by  $\omega$  to reveal its  $\omega \rightarrow 0$  asymptotics.

For twisted bilayer graphene described by the continuum model, we expect a combination of both features, because of the unbounded linear dispersion of Dirac Fermions and the superlattice structure of the Moiré-pattern. From figure 2 we see that the DOS is characterized by a van Hove singularity followed by a ‘real’ step-like singularity which is repeated to higher doping levels. This pseudo-gap structure divides the spectrum in several bands and will be followed by the Drude weight. Nevertheless, these modulations are superposed onto a constant linear background as suggested by the unbounded continuum model.

The  $\mu$  dependence of the Drude weight  $D(\mu)$  in units of  $2D_0$  is presented in figure 7 for two large twist angles. As is apparent, for small chemical potential  $D(\mu)$  follows twice the monolayer value  $2D_0$  independent of the twist angle, as expected for Dirac systems. For larger  $\mu$ , the Drude weight drops and remains less than  $2D_0$  until it converges to the uncoupled bilayer system for  $\mu \gg \gamma_0$ .

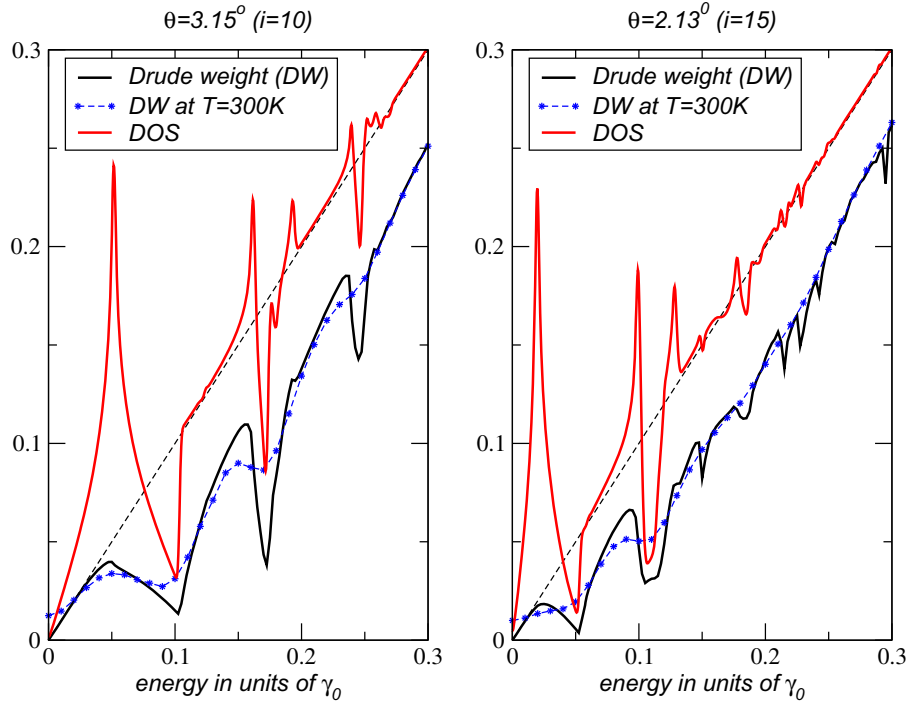


**Figure 7.** Drude weight  $D$  as a function of chemical potential  $\mu$  for two different twist angles (black curve), together with the corresponding DOS (red curve). The thin dashed line corresponds to the Drude weight and DOS of two decoupled monolayers, in units of  $2D_0$ , equation (13), and  $\rho_0 = \frac{4\gamma_0}{\pi(\hbar v_F)^2}$ , respectively. Symbols (blue  $\star$ ) resemble the Drude weight at  $T = 300$  K.

As outlined above,  $D(\mu)$  exhibits dips that accurately correlate with dips in the DOS, also shown in figure 7 (red). The resulting picture suggests the above mentioned approximate shell structure, albeit (in general) without gaps between shells, just as the suppressed DOS. The first shell can be fairly well approximated by the hexagonal tight-binding model.

At finite temperature  $T = 300$  K (and also for disorder), the Drude weight is smeared out for large twist angle  $i = 10$ , thus reaffirming the interpretation of the repeated shell-structure. Nevertheless, the shell structure becomes less pronounced with smaller  $\theta$  which is also reflected by its temperature response.

For small angles, the Drude weight provides a sensitive fingerprint for the breakdown of Dirac physics that occurs around the magical angles due to the emergence of flat bands. This can be seen on the right hand side of figure 8 for small angles above ( $i = 26$ ) and below ( $i = 36$ ) the critical angle. The Drude weight becomes *larger* than the Drude weight of two monolayers before it drops indicating the band width of the flat band. At the critical angle ( $i = 31$ ), this band width becomes zero, and interestingly, the scaling of  $D_0$  is recovered. Note that for  $i = 26$ , we find a transport gap  $D = 0$  at finite chemical potential  $\mu = 0.06\gamma_0$ .

The increase of the band width for twist angles larger than  $\theta_1^m$  can be nicely appreciated from the Drude weight. This becomes considerably more difficult from the DOS, displayed on the left hand side of figure 8. The reason for this is that the Drude weight is obtained from integrating over the whole spectral region and not only from the low energy band structure.

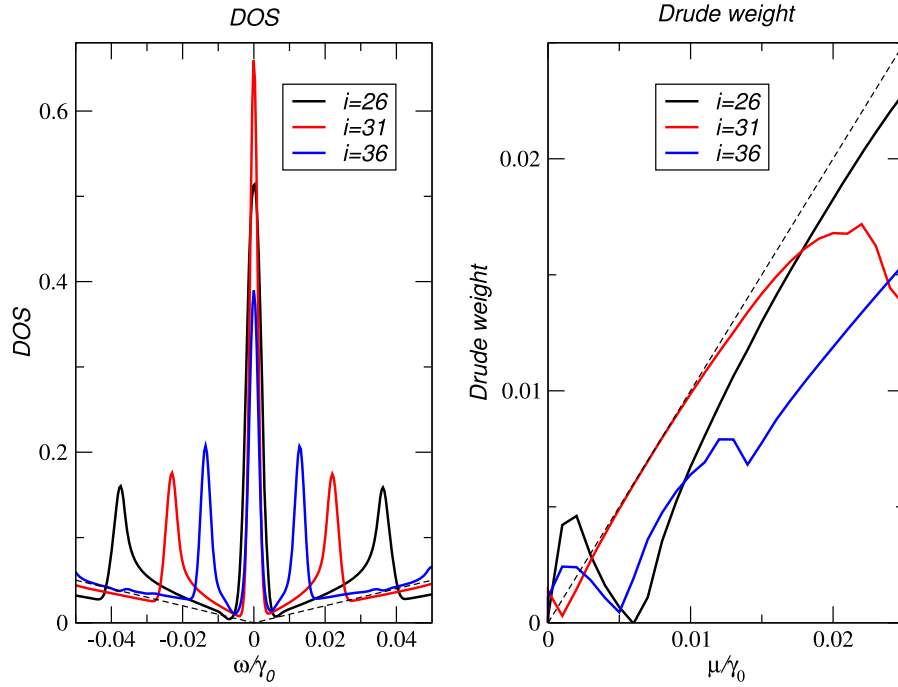


**Figure 8.** The DOS (left) and the Drude weight (right) around the first critical angle  $\theta = 1.05^\circ$  ( $i = 31$ ) in units of figure 7. Dashed lines correspond to uncoupled bilayer.

Nevertheless, the weight of the peak at zero energy is maximal at the magic angle (red curve), indicating its singularity.

## 6. Plasmons

A complementary aspect to the optical absorption is the plasmon excitation spectrum of the electron gas. Conceptually, a plasmon is an oscillating charge density mode (hence accompanied by an oscillating electric potential), which is sustained by the Coulomb interactions between electrons. The dispersion relation of these modes is given by the zeroes of the dielectric function  $\epsilon(\mathbf{q}, \omega) = 0$ , that relates the screened electric potential  $V_{\text{sc}}(\mathbf{r}, t)$  to an externally applied potential  $V_{\text{ext}}(\mathbf{r}, t)$ ,

$$V_{\text{sc}}(\mathbf{q}, \omega) = \frac{V_{\text{ext}}(\mathbf{q}, \omega)}{\epsilon(\mathbf{q}, \omega)}.$$

A plasmon is, therefore, a finite solution  $V_{\text{sc}}(\mathbf{q}, \omega)$  that requires no external driving, i.e. it is self-sustained. A Landau-damped plasmon corresponds to a *peak* in  $1/\epsilon(\mathbf{q}, \omega)$ , and decays due to dissipation into particle-hole excitations.

The dielectric function  $\epsilon(\mathbf{q}, \omega)$  may be computed within the random phase approximation (RPA). In the long-wavelength limit, we may thus relate  $\epsilon_{\text{RPA}}$  directly to  $\sigma(\omega)$  using equation (6),

$$\epsilon_{\text{RPA}}(\mathbf{q}, \omega) \approx 1 + \frac{i}{2\epsilon_0\epsilon} \frac{|\mathbf{q}|}{\omega} \sigma(\omega) = 1 + i \frac{\pi\alpha_g}{2\epsilon} \frac{v_F|\mathbf{q}|}{\omega} \frac{\sigma(\omega)}{\sigma_0}, \quad (21)$$



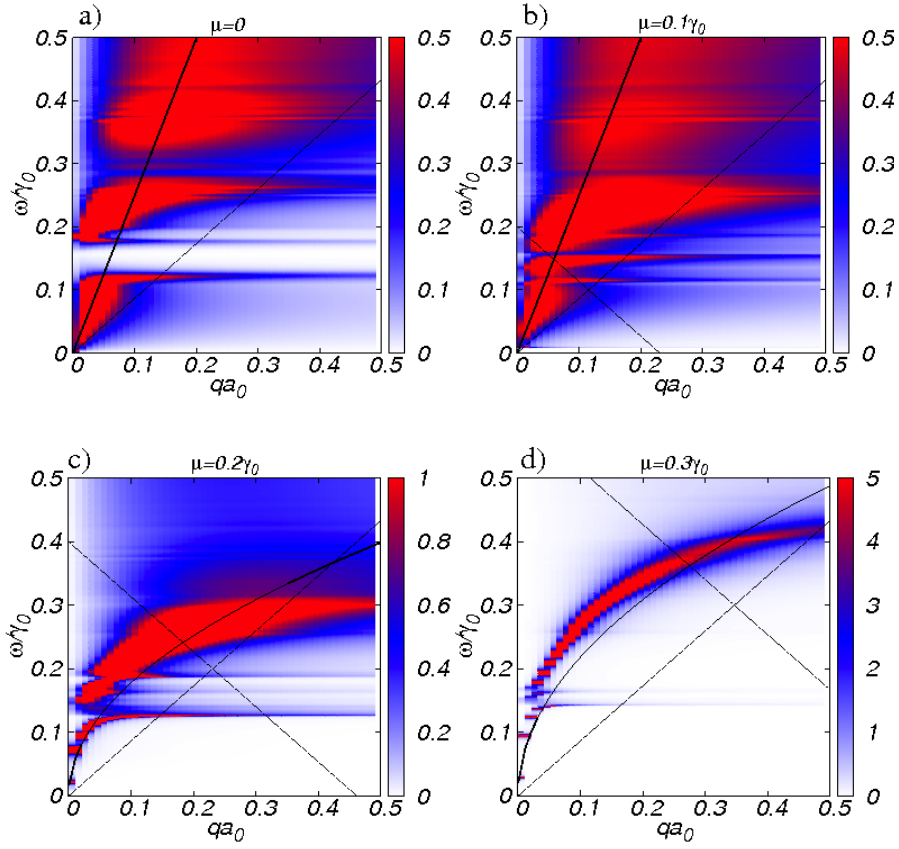


**Figure 9.** Loss function  $S(\mathbf{q}, \omega) = -\text{Im} \epsilon^{-1}(\mathbf{q}, \omega)$  in the long-wavelength RPA approximation for  $\theta = 3.15^\circ$  ( $i = 10$ ) and  $\epsilon = 2.4$ . The dashed curved line corresponds to the undamped plasmon of the decoupled bilayer. The region of undamped plasmons of the decoupled bilayer is defined by straight lines.

where  $\alpha_g = e^2/(4\pi\epsilon_0\hbar v_F) \approx 2.2$  is graphene's fine structure constant. In equation (21) we have neglected corrections due to the finite interlayer distance, and consider that interlayer and intralayer electron–electron interaction are of the same form  $\sim 1/q$ . In this approximation all the collective modes correspond to charge excitations in which the charge oscillates in phase in the two layers [39, 40].

To compute  $\omega_p$  for small frequencies, we may expand  $\text{Im} \sigma$  in equation (19) by the Drude term,  $\text{Im} \sigma(\omega) \approx \frac{D}{\omega}$ . This results in the dispersion of a classical 2D plasmon

$$\omega_p \approx \sqrt{\frac{D|q|}{2\epsilon_0\epsilon}}. \quad (22)$$

For two decoupled monolayers, one just replaces  $D = 8\mu/\pi\hbar\sigma_0$  above, which is shown as dotted curved line in figures 9 and 10.

### 6.1. Plasmons in twisted bilayer

In twisted graphene bilayer there may exist four types of plasmonic modes or resonances: (i) undamped (conventional) graphene plasmons for chemical potentials with  $\mu \ll \epsilon_M$ ;

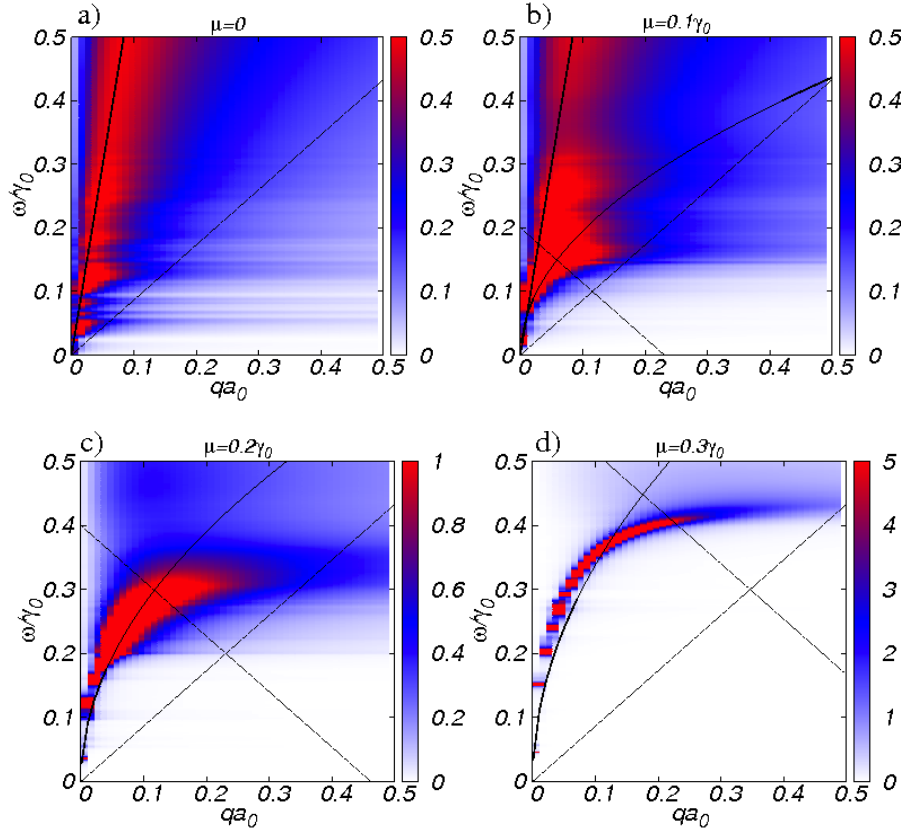


**Figure 10.** Loss function  $S(\mathbf{q}, \omega)$  like in figure 9, for the first magic angle  $\theta = \theta_1^m = 1.05^\circ$  ( $i = 31$ ) and  $\epsilon = 1$ .

(ii) interband ‘plasmons’ present also for  $\mu = 0$ ; (iii) damped plasmons for large chemical potential  $\mu \gg \epsilon_M$ ; and (iv) transverse plasmons. Below, we will briefly outline the main properties of these different types.

**6.1.1. Undamped plasmons.** At low doping, there exists a low energy window with  $\text{Re } \sigma = 0$  that gives rise to undamped plasmons governed by the Drude weight  $D$ . In this regime, the twisted bilayer can be described by linear Dirac Fermions and  $D(\mu)$  follows the Drude weight of the uncoupled system  $2D_0$ , as shown in figure 7. This energy window becomes smaller for decreasing twist angle since the van Hove singularity moves closer to the neutrality point and is only relevant for large angles.

**6.1.2. Interband plasmons.** In monolayer graphene, a peak in the loss function associated to  $\pi \rightarrow \pi^*$  transitions around the van Hove singularity and with linear dispersion was first predicted by DFT-studies [41], and later experimentally observed in suspended graphene by electron energy-loss spectroscopy [42]. Within the hexagonal tight-binding model and RPA, i.e. without including correlation or renormalization effects, no zero of the dielectric function is obtained [43]. The absorption peak would thus be merely due to interband transitions enhanced by a band-structure effect; nevertheless, in bi- or multilayer,  $\epsilon^{\text{RPA}}(\mathbf{q}, \omega)$  becomes zero around the  $M$  point [44]. In the twisted graphene bilayer, there exist several van Hove singularities such

that interband plasmons (or absorption enhancement) are to be expected. These are especially dominate for large twist angle and can lead to a broad optical gap in the interband excitations where  $\text{Im } \sigma < 0$ .

**6.1.3. Damped plasmons.** In the regime of large chemical potential,  $\mu \gg \epsilon_M$ , the conventional intraband plasmon is recovered, albeit Moiré-damped. This can be deduced from figure 6 which will be used to discuss the plasmon dispersion in terms of the loss function. The dispersion only depends slightly on the twist angle and becomes well-defined for large  $\mu$ , extending into the Landau damped region just as for the monolayer.

**6.1.4. Transverse plasmons.** There is also the possibility for transverse or transverse electromagnetic (TE) plasmons modes given by the condition [45]

$$1 - \frac{\omega i \sigma(\omega)}{c^2 \sqrt{q^2 - \omega^2/c^2}} = 0. \quad (23)$$

For TE modes, the plasmon dispersion is closely pinned to the light cone which justifies our local approximation ( $q \rightarrow 0$ ) and there are (damped) solutions to equation (23) if  $\text{Im } \sigma < 0$ . Since they can only exist in twisted bilayer surrounded by a homogeneous dielectric background [46], we will not discuss them any further.

## 6.2. Loss function

The loss function, defined as  $S(\mathbf{q}, \omega) = -\text{Im } \epsilon^{-1}(\mathbf{q}, \omega)$  is a measure of the spectral density of plasmon excitations. Thus, a sharp peak in  $S(\mathbf{q}, \omega)$  reveals a long-lived (transverse magnetic (TM)) plasmon of that frequency and momentum. A proper undamped plasmon, defined by  $\epsilon(\mathbf{q}, \omega) = 0$ , corresponds to a delta peak in  $S(\mathbf{q}, \omega)$ , since  $\epsilon^{-1}(\mathbf{q}, \omega)$  satisfies Kramers–Kronig relations.

In figure 9, we present  $S(\mathbf{q}, \omega)$  within the long-wavelength RPA approximation of equation (21) at intermediate angle  $\theta = 3.15^\circ$  ( $i = 10$ ) for different chemical potential with  $\epsilon = 2.4$ . In figure 10, the same quantity is shown at the first magic angle  $\theta = \theta_1^m = 1.05^\circ$  ( $i = 31$ ) with  $\epsilon = 1$ . In all plots, the Dirac dispersion  $\omega = v_F q$  and the  $\hbar\omega = 2E_F - \hbar v_F q$  from figure 5 is shown as dashed lines, indicating the onset of intra- and interband transitions.

The qualitative features of the plasmon spectrum in both behavior can be deduced from figure 6. For zero or low chemical potential (figures 9(a) and 10(a)), the loss function reveals an acoustic interband ‘plasmon’ with sound velocity  $v_s \approx \pi \alpha_g v_F / \epsilon$  (solid line). It is not a plasmon in the conventional sense, since the dielectric function does not become zero. This linear (interband) mode crosses over to the conventional  $\sqrt{q}$  (intraband) mode, figures 9, 10(b) and (c), and becomes well-defined for large chemical potential, figures 9, 10(d), although there are slight variations compared to equation (22) shown as solid curved line. Note that for twisted bilayer on a substrate (e.g.  $\epsilon \approx 2.4$ ), the local approximation of the conductivity needs to be improved for large chemical potential and low twist angle since there is considerable weight of the plasmon mode in the intraband particle–hole continuum for large  $q$ . In single-layer graphene, this is forbidden due to the square-root singularity of  $\sigma(q, \omega)$  at  $\omega = v_F q$ .

The loss function also exhibits a pronounced optical gap in the region where  $\text{Im } \sigma < 0$ . This feature is especially visible at larger angles (figure 9). The gap is a consequence of the van Hove singularity, and is perhaps the most visible effect on the plasmon response of the Moiré

pattern at large  $\theta$ . Secondary van Hoves give rise to additional gaps at higher frequencies. At smaller angles, the gap is smaller and less defined, although some hints of it persist down to the first magic angle, specially close to  $\mu = 0$  (figure 10(a)).

## 7. Conclusions

We have analyzed the DOS, optical conductivity, Drude weight and plasmon spectrum in a twisted bilayer for various angles, doping levels and temperature, and compared them to the uncoupled system. We have found a universal low-frequency conductivity and peaks at finite frequency that correlate to van Hove singularities in the DOS. These latter features, however, become scrambled at decreasing angles. We have also shown that the Drude weight in twisted bilayers is usually below that of two decoupled monolayers,  $2D_0$ , and exhibits a shell-like structure, following again van Hove singularities in the DOS. Only for small angles close to the neutrality point, the Drude weight becomes larger than  $2D_0$ , signaling the emergence of a flat band. The Drude weight resembles a sensitive quantity to numerically distinguish the different electronic structure at critical angles since it is obtained from integrating over the whole spectrum and is directly related to transport experiments. We have finally discussed how plasmons may become damped by the interlayer Moiré coupling which opens up new dissipation channels. Significant spectral structure survives, however, including undamped plasmons and multiple long-lifetime resonances (interband plasmons) within the extended interband particle-hole continuum.

## Acknowledgments

We thank G Gómez-Santos and E Prada for discussions. This work has been supported by FCT under grants PTDC/FIS/101434/2008; PTDC/FIS/113199/2009, by MIC-Spain under grant FIS2010-21883-C02-02, FIS2011-23713 and FIS2012-33521, and by the European Research Council Advanced grant, contract 290846.

## References

- [1] Nair R R, Blake P, Grigorenko A N, Novoselov K S, Booth T J, Stauber T, Peres N M R and Geim A K 2008 Fine structure constant defines visual transparency of graphene *Science* **320** 1308
- [2] Mak K F, Sfeir M Y, Wu Y, Lui C H, Misewich J A and Heinz T F 2008 Measurement of the optical conductivity of graphene *Phys. Rev. Lett.* **101** 196405
- [3] Falkovsky L A and Pershoguba S S 2007 Optical far-infrared properties of a graphene monolayer and multilayer *Phys. Rev. B* **76** 153410
- [4] Stauber T, Peres N M R and Geim A K 2008 Optical conductivity of graphene in the visible region of the spectrum *Phys. Rev. B* **78** 085432
- [5] Avouris P 2010 Graphene: electronic and photonic properties and devices *Nano Lett.* **10** 4285–94
- [6] Bonaccorso F, Sun Z, Hasan T and Ferrari A C 2010 Graphene photonics and optoelectronics *Nature Photon.* **4** 611–22
- [7] Koppens F H L, Chang D E and García de Abajo J F 2011 Graphene plasmonics: a platform for strong light-matter interactions *Nano Lett.* **11** 3370–7
- [8] Yang L, Deslippe J, Park C-H, Cohen M L and Louie S G 2009 Excitonic effects on the optical response of graphene and bilayer graphene *Phys. Rev. Lett.* **103** 186802

- [9] Kravets V G, Grigorenko A N, Nair R R, Blake P, Anissimova S, Novoselov K S and Geim A K 2010 Spectroscopic ellipsometry of graphene and an exciton-shifted van Hove peak in absorption *Phys. Rev. B* **81** 155413
- [10] Vafeek O 2006 Thermoplasma polariton within scaling theory of single-layer graphene *Phys. Rev. Lett.* **97** 266406
- [11] Liu M, Yin X, Ulin-Avila E, Geng B, Zentgraf T, Ju L, Wang F and Zhang X 2011 A graphene-based broadband optical modulator *Nature* **474** 64
- [12] Wunsch B, Stauber T, Sols F and Guinea F 2006 Dynamical polarization of graphene at finite doping *New J. Phys.* **8** 318
- [13] Hwang E H and Das Sarma S 2007 Dielectric function, screening and plasmons in two-dimensional graphene *Phys. Rev. B* **75** 205418
- [14] Ju *et al* 2012 Graphene plasmonics for tunable terahertz metamaterials *Nature Nanotechnol.* **6** 630
- [15] Chen J *et al* 2012 Optical nano-imaging of gate-tunable graphene plasmons *Nature* **487** 77
- [16] Fei Z *et al* 2012 Gate-tuning of graphene plasmons revealed by infrared nano-imaging *Nature* **487** 82
- [17] Abergel D S L and Fal'ko V I 2007 Optical and magneto-optical far-infrared properties of bilayer graphene *Phys. Rev. B* **75** 155430
- [18] Campos-Delgado J, Algara-Siller G, Santos C N, Kaiser U and Raskin J-P 2013 Twisted bi-layer graphene: microscopic rainbows *Small* **9** 3247
- [19] Moon P and Koshino M 2013 Optical absorption in twisted bilayer graphene *Phys. Rev. B* **87** 205404
- [20] Tabert C J and Nicol E J 2013 Optical conductivity of twisted bilayer graphene *Phys. Rev. B* **87** 121402
- [21] Lopes dos Santos J M B, Peres N M R and Castro Neto A H 2012 Continuum model of the twisted graphene bilayer *Phys. Rev. B* **86** 155449
- [22] Mele E J 2010 Commensuration and interlayer coherence in twisted bilayer graphene *Phys. Rev. B* **81** 161405
- [23] dos Santos J M B L, Peres N M R and Castro Neto A H 2007 Graphene bilayer with a twist: electronic structure *Phys. Rev. Lett.* **99** 256802
- [24] San-Jose P, González J and Guinea F 2012 Non-abelian gauge potentials in graphene bilayers *Phys. Rev. Lett.* **108** 216802
- [25] Castro E V, Novoselov K S, Morozov S V, Peres N M R, Lopes dos Santos J M B, Nilsson J, Guinea F, Geim A K and Castro Neto A H 2007 Biased bilayer graphene: semiconductor with a gap tunable by the electric field effect *Phys. Rev. Lett.* **99** 216802
- [26] Suárez Morell E, Correa J D, Vargas P, Pacheco M and Barticevic Z 2010 Flat bands in slightly twisted bilayer graphene: tight-binding calculations *Phys. Rev. B* **82** 121407
- [27] Bistritzer R and MacDonald A H 2011 Moiré bands in twisted double-layer graphene *Proc. Natl Acad. Sci. USA* **108** 12233–7
- [28] Li G, Luican A, Lopes dos Santos J M B, Castro Neto A H, Reina A, Kong J and Andrei E Y 2010 Observation of van Hove singularities in twisted graphene layers *Nature Phys.* **6** 109–13
- [29] Luican A, Li G, Reina A, Kong J, Nair R R, Novoselov K S, Geim A K and Andrei E Y 2011 Single-layer behavior and its breakdown in twisted graphene layers *Phys. Rev. Lett.* **106** 126802
- [30] Yan W, Liu M, Dou R-F, Meng L, Feng L, Chu Z-D, Zhang Y, Liu Z, Nie J-C and He L 2012 Angle-dependent van Hove singularities in a slightly twisted graphene bilayer *Phys. Rev. Lett.* **109** 126801
- [31] Brihuega I, Mallet P, González-Herrero H, Trambly de Laissardière G, Ugeda M M, Magaud L, Gómez-Rodríguez J M, Ynduráin F and Veuillen J-Y 2012 Unraveling the intrinsic and robust nature of van Hove singularities in twisted bilayer graphene by scanning tunneling microscopy and theoretical analysis *Phys. Rev. Lett.* **109** 196802
- [32] Giuliani G and Vignale G 2005 *Quantum Theory of the Electron Liquid* 1st edn (Cambridge: Cambridge University Press)
- [33] Stauber T and Gómez-Santos G 2010 Dynamical current–current correlation of the hexagonal lattice and graphene *Phys. Rev. B* **82** 155412
- [34] Gusynin V P, Sharapov S G and Carbotte J P 2007 Sum rules for the optical and Hall conductivity in graphene *Phys. Rev. B* **75** 165407

- [35] Abedinpour S H, Vignale G, Principi A, Polini M, Tse W-K and MacDonald A H 2011 Drude weight, plasmon dispersion and ac conductivity in doped graphene sheets *Phys. Rev. B* **84** 045429
- [36] Sabio J, Nilsson J and Castro Neto A H 2008  $f$ -sum rule and unconventional spectral weight transfer in graphene *Phys. Rev. B* **78** 075410
- [37] Peres N M R and Stauber T 2008 Transport in a clean graphene sheet at finite temperature and frequency *Int. J. Mod. Phys. B* **22** 2529–36
- [38] Falkovsky L A and Varlamov A A 2007 Space–time dispersion of graphene conductivity *Eur. Phys. J. B* **56** 281–4
- [39] Borghi G, Polini M, Asgari R and MacDonald A H 2009 Dynamical response functions and collective modes of bilayer graphene *Phys. Rev. B* **80** 241402
- [40] Profumo R E V, Polini M, Asgari R, Fazio R and MacDonald A H 2010 Electron–electron interactions in decoupled graphene layers *Phys. Rev. B* **82** 085443
- [41] Kramberger C *et al* 2008 Linear plasmon dispersion in single-wall carbon nanotubes and the collective excitation spectrum of graphene *Phys. Rev. Lett.* **100** 196803
- [42] Eberlein T, Bangert U, Nair R R, Jones R, Gass M, Bleloch A L, Novoselov K S, Geim A and Briddon P R 2008 Plasmon spectroscopy of free-standing graphene films *Phys. Rev. B* **77** 233406
- [43] Stauber T, Schliemann J and Peres N M R 2010 Dynamical polarizability of graphene beyond the Dirac cone approximation *Phys. Rev. B* **81** 085409
- [44] Yuan S, Roldán R and Katsnelson M I 2011 Excitation spectrum and high-energy plasmons in single-layer and multilayer graphene *Phys. Rev. B* **84** 035439
- [45] Mikhailov S A and Ziegler K 2007 New electromagnetic mode in graphene *Phys. Rev. Lett.* **99** 016803
- [46] Kotov O V, Kol’chenko M A and Lozovik Y E 2013 Ultrahigh refractive index sensitivity of TE-polarized electromagnetic waves in graphene at the interface between two dielectric media *Opt. Express* **21** 13533–46